

Orbital and spin interplay in spin-gap formation in pyroxene titanium oxides $ATiSi_2O_6$ ($A=Na, Li$)

Toshiya Hikiyara and Yukitoshi Motome
 RIKEN, 2-1 Hirosawa, Wako, Saitama 351-0198, Japan
 (Dated: December 2, 2024)

Interplay between orbital and spin degrees of freedom is theoretically studied for the phase transition to the spin-singlet state with lattice dimerization in pyroxene titanium oxides $ATiSi_2O_6$ ($A=Na, Li$). For the quasi one-dimensional spin-1/2 systems, we derive an effective spin-orbital-lattice coupled model in the strong correlation limit with explicitly taking account of the t_{2g} orbital degeneracy, and investigate the model by numerical simulation as well as the mean-field analysis. We find a nontrivial feedback effect between orbital and spin degrees of freedom; as temperature decreases, development of antiferromagnetic spin correlations changes the sign of orbital correlations from antiferro to ferro type, and finally the ferro-type orbital correlations induce the dimerization and the spin-singlet formation. As a result of this interplay, the system undergoes a finite-temperature transition to the spin-dimer and orbital-ferro ordered phase concomitant with the Jahn-Teller lattice distortion. The nontrivial interplay between orbital and spin also leads to a deviation from the Curie-Weiss behavior of the magnetic susceptibility. The numerical results for realistic values of parameters well reproduce the experimental data. The results reveal that the Jahn-Teller energy scale is considerably small and the orbital and spin exchange interactions play a decisive role in the present system.

PACS numbers: 75.30.Et, 75.10.Jm, 75.40.Cx

I. INTRODUCTION

Orbital degree of freedom has attracted much attention since it plays key roles in electronic properties of transition metal compounds.^{1,2} The orbital degree of freedom couples with the Jahn-Teller (JT) lattice distortion, and in many compounds, the energy scale of the JT stabilization energy is larger than that of the spin and orbital exchange interactions.³ A typical example is the mother compound of colossal magnetoresistive (CMR) manganites, $LaMnO_3$: The JT energy scale is $\sim 1eV$ and the spin exchange energy scale is $\sim 10meV$. Consequently, the orbital-lattice transition occurs at a much higher temperature ($\sim 800K$) than the antiferromagnetic (AF) transition temperature ($\sim 140K$).⁴ In these systems, the orbital-lattice physics is dominant, and the orbital and lattice orderings modify the spin exchange interaction to lead a magnetic ordering in a secondary effect. Moreover, the JT distortion suppresses fluctuation effects in orbital and spin degrees of freedom. Hence, a large JT coupling masks bare interplay between spin and orbital in many real materials.

Quantum and thermal fluctuations in the competition between the spin and orbital exchange interactions may yield novel phenomena, and therefore, it is highly desired to explore systems in which the genuine spin-orbital interplay appears explicitly. One of promising candidates is the t_{2g} electron system such as titanium and vanadium oxides. In t_{2g} systems, the JT coupling becomes smaller than in the e_g systems such as CMR manganites because spatial shapes of t_{2g} orbitals avoid directions of surrounding ligands in the octahedral positions. For instance, in vanadium perovskite oxides AVO_3 ($A=La, Ce$), the orbital-lattice transition temperature becomes

FIG. 1: Skew edge-sharing chain structure of TiO_6 octahedra in pyroxene oxides $ATiSi_2O_6$ ($A=Na, Li$). The lattice structure consists of the chains weakly coupled with each other. Balls in the center of each octahedron denote Ti ions, and oxygen ions are on the corners of the octahedra. The octahedra share their edges in the xy and yz planes alternatively. White objects with four lobes denote d_{xy} and d_{yz} orbitals of t_{2g} electrons, and t^{11} (t^{22}) is the σ -bond overlap integrals between d_{xy} (d_{yz}) orbitals. See the text for details.

even lower than the AF one,⁵ and novel interplay between spin and orbital is proposed theoretically.^{6,7}

Pyroxene titanium oxides $ATiSi_2O_6$ ($A=Na, Li$) are typical examples of the t_{2g} electron systems where such interplay between spin and orbital is expected.⁸ The lattice structure of these compounds consists of characteristic one-dimensional (1D) chains of skew edge-sharing TiO_6 octahedra as shown in Fig. 1. There, the edges of octahedra in the xy and yz planes are alternatively shared between neighboring octahedra, which leads to the zig-zag structure. Each magnetic Ti^{3+} ion has one d electron in these insulating materials. The TiO_6 chains are bridged by SiO_4 tetrahedra, and therefore, the inter-chain coupling is considered to be much weaker than the intrachain interaction. Hence, we may consider that a quasi 1D spin-1/2 system is realized.

Pyroxene titanium oxides show a peculiar phase transition. The magnetic susceptibility shows a sharp drop at $T_c = 210K$ and $230K$ in $NaTiSi_2O_6$ and $LiTiSi_2O_6$, respectively, which indicates the transition to a spin-singlet state with a finite spin gap.⁸ Below T_c , a dimerization of Ti-Ti distances along the chain was observed by the X-ray scattering.⁹ These remind us of a spin-Peierls transition.¹⁰ However, above T_c , the magnetic

susceptibility shows an unusual temperature dependence which clearly deviates from that of other spin-Peierls compounds. In spin-Peierls systems, the dimerization is caused by the magnetoelastic coupling, and therefore, the transition occurs when short-range spin correlations develop enough to drive the lattice dimerization. This development of spin correlations is manifested in a broad peak of the magnetic susceptibility above T_c , and the peak temperature gives a rough estimate of the spin exchange energy scale. Contrary to this conventional behavior, the magnetic susceptibility of the pyroxene compounds at high temperatures increases as temperature decreases, and suddenly drops at T_c without a clear formation of the broad peak.⁸ This suggests a breakdown of the simple spin-Peierls picture in these pyroxene compounds.

For the peculiar transition to the spin-singlet state, an importance of the t_{2g} orbital degree of freedom has been pointed out.⁸ Theoretically, a scenario of the orbital-driven spin-singlet formation has been explored in spin-orbital coupled models for t_{2g} electron systems.¹¹ It was proposed that the orbital ordering may modify effective spin exchange interactions and induce the spin-singlet formation. However, models were considered only for systems with the corner-sharing octahedra, and hence, it is unclear that the argument is applicable to the present pyroxene systems with the edge-sharing octahedra. For the present systems, a similar scenario has been proposed,¹² however, the analysis was heuristic and not sufficient to conclude the mechanism of the finite-temperature transition in the present compounds. In order to clarify the nature of the transition and the low-temperature phase, we need more elaborate analysis. In particular, it is indispensable to investigate thermodynamic properties on the basis of a microscopic model.

In the present study, we will theoretically explore the mechanism of the unusual phase transition in the pyroxene titanium oxides $ATiSi_2O_6$ explicitly taking account of the t_{2g} orbital degree of freedom. We derive an effective spin-orbital-lattice coupled model in the strong correlation limit, and investigate thermodynamics as well as the ground-state properties of the model applying the numerical quantum transfer matrix method and mean-field-type arguments. As a result, we find that interesting interplay between orbital and spin degrees of freedom occurs in the system, and the interplay gives a comprehensive understanding of the peculiar properties of the pyroxene compounds: Although both orbital and spin correlations are antiferro type at high temperatures, development of AF spin correlations with decreasing temperature yields a sign change of orbital correlations from antiferro to ferro type. After the sign change, the ferro-type orbital correlations grow with the antiferro-type spin correlations, and finally, induce the spin-singlet formation with a dimerization. Furthermore, the nontrivial temperature dependence of orbital correlations modifies an effective magnetic coupling, and results in a non Curie-Weiss behavior of the magnetic susceptibility. We show

that our model with realistic parameters reproduces the peculiar temperature dependence of the magnetic susceptibility in experiment.

The organization of this paper is as follows. In the following section II, applying the strong-coupling approach, we derive an effective spin-orbital-lattice coupled model for the t_{2g} pyroxene compounds $ATiSi_2O_6$. In Sec. III, we discuss properties of the system in the ground state and in the high-temperature limit using a mean-field type argument. In Sec. IV, we study thermodynamic properties of the effective model by numerical simulations. We describe the method in Sec. IV A. The numerical results are shown in Sec. IV B. Temperature dependences of the magnetic susceptibility and the spin and orbital correlations are discussed. We also compare our result of the magnetic susceptibility with the experimental data. Finally, Section V is devoted to summary and concluding remarks.

II. MODEL HAMILTONIAN

In this section, we derive an effective spin-orbital-lattice coupled model for the pyroxene oxides $ATiSi_2O_6$, whose Hamiltonian reads

$$\mathcal{H} = \mathcal{H}_{so} + \mathcal{H}_{JT} + \mathcal{H}_{\perp}. \quad (1)$$

The first term describes the intersite exchange interactions in spin and orbital degrees of freedom, and the second term includes the Jahn-Teller type orbital-lattice coupling. These two are defined within each 1D chain. The third term describes the interchain coupling.

The spin-orbital exchange Hamiltonian \mathcal{H}_{so} is derived from a t_{2g} multiorbital Hubbard model by using the perturbation in the strong correlation limit.^{3,13} The skew structure shown in Fig. 1 distorts TiO_6 octahedra in the form that four Ti-O bonds in which the oxygen ions are shared with neighboring TiO_6 octahedra are longer than the rest two Ti-O bonds in each octahedron.⁹ The distortion leads to the splitting of threefold t_{2g} levels into a low-lying doublet with d_{xy} and d_{yz} orbitals and a single d_{zx} level when we take the coordinates as shown in Fig. 1. The splitting is estimated as ~ 300 meV in a pyroxene vanadium oxide which has a similar lattice structure.¹⁴ Because of this level splitting, it is reasonable to start from the 1D Hubbard model with twofold degeneracy of d_{xy} and d_{yz} orbitals with tracing out the higher d_{zx} level. The Hamiltonian is given in the form

$$\begin{aligned} \mathcal{H}_{Hub} = & \sum_{i,j} \sum_{\alpha,\beta} \sum_{\tau} (t_{ij}^{\alpha\beta} c_{i\alpha\tau}^{\dagger} c_{j\beta\tau} + \text{H.c.}) \\ & + \frac{1}{2} \sum_i \sum_{\alpha,\beta,\alpha'\beta'} \sum_{\tau\tau'} U_{\alpha\beta,\alpha'\beta'} c_{i\alpha\tau}^{\dagger} c_{i\beta\tau'}^{\dagger} c_{i\beta'\tau'} c_{i\alpha'\tau}, \end{aligned} \quad (2)$$

where i, j are site indices within the 1D chain, τ, τ' are spin indices, and $\alpha, \beta = 1$ (d_{xy}) and 2 (d_{yz}) are orbital indices. The first term describes the electron hopping, and

the second term denotes the onsite Coulomb interactions where we use the standard parametrizations,

$$U_{\alpha\beta,\alpha'\beta'} = U'\delta_{\alpha\alpha'}\delta_{\beta\beta'} + J_H(\delta_{\alpha\beta'}\delta_{\beta\alpha'} + \delta_{\alpha\beta}\delta_{\alpha'\beta'}), \quad (3)$$

$$U = U_{11,11} = U_{22,22} = U' + 2J_H. \quad (4)$$

Here, we neglect the relativistic spin-orbit coupling.

The perturbation calculation is performed in the strong correlation limit $t_{ij}^{\alpha\beta} \ll U, U', J_H$ by taking an atomic eigenstate with one electron at each site. In the edge-sharing configuration as shown in Fig. 1, the most relevant contribution in the transfer integrals $t_{ij}^{\alpha\beta}$ is the overlap between the nearest-neighbor (NN) pairs with the same orbitals within the same plane, which are called the σ bonds. The σ -bond overlap integrals are $t_{i,i+1}^{11}$ for NN pairs in the xy plane and $t_{i,i+1}^{22}$ for those in the yz plane as shown in Fig. 1. These two types of the overlap integrals take the same value, and we denote them by t_σ , i.e., $t^{11} = t^{22} = t_\sigma$ in the following. Other transfer integrals are much smaller than t_σ ; in particular, $t_{i,i+1}^{12} = t_{i,i+1}^{21} = 0$ between NN sites from the symmetry. In the present study, we take account of the σ -bond contributions only, and neglect other transfer integrals.¹⁵ The approximation is known to give a reasonable result for spinel oxides which also have edge-sharing network of octahedra.¹⁶ Note that the transfer integral t_σ is diagonal in the orbital sector, i.e., it does not mix different orbitals. This leads to the Ising nature of the orbital isospin interaction in the following effective model.

The second order perturbation in t_σ gives the effective spin-orbital Hamiltonian in the form

$$\mathcal{H}_{\text{so}} = -J \sum_i (h_{i,i+1}^{\text{oAF}} + h_{i,i+1}^{\text{oF}}), \quad (5)$$

$$h_{i,i+1}^{\text{oAF}} = (A + B\mathbf{S}_i \cdot \mathbf{S}_{i+1}) \left(\frac{1}{2} - 2T_i T_{i+1} \right), \quad (6)$$

$$h_{i,i+1}^{\text{oF}} = C \left(\frac{1}{4} - \mathbf{S}_i \cdot \mathbf{S}_{i+1} \right) \left(\frac{1}{2} \pm T_i \right) \left(\frac{1}{2} \pm T_{i+1} \right), \quad (7)$$

where \mathbf{S}_i is the $S = 1/2$ spin operator at site i and T_i is the Ising isospin which describes the orbital state at site i as $T_i = +1/2(-1/2)$ when the d_{xy} (d_{yz}) orbital is occupied. The signs in Eq. (7) take $+$ ($-$) for the bonds within the xy (yz) plane. The coupling constants in Eqs. (5)-(7) are given by parameters in Eq. (2) as

$$J = \frac{(t_\sigma)^2}{U}, \quad (8)$$

$$A = \frac{3}{4(1-3\eta)} + \frac{1}{4(1-\eta)}, \quad (9)$$

$$B = \frac{1}{1-3\eta} - \frac{1}{1-\eta}, \quad (10)$$

$$C = \frac{4}{3} \left(\frac{1}{1+\eta} + \frac{2}{1-\eta} \right), \quad (11)$$

$$\eta = \frac{J_H}{U}, \quad (12)$$

where we use Eq. (4). The realistic value of η will be estimated as $\eta \sim 0.1$ later. Therefore, we consider that A, B , and C are all positive in the following.

We note that a part of the spin-orbital interactions, i.e., $h_{i,i+1}^{\text{oF}}$ in Eq. (7) takes a similar form to the model proposed in Ref. 12. Our model derived from the multi-orbital Hubbard model contains both ferro and anti-ferro types of orbital interactions as well as the nontrivial contributions which are missed in the previous model in Ref. 12. We will show that these factors in the present model play important roles in the thermodynamics. In particular, as shown in the following, our model exhibits a nontrivial temperature dependence of orbital isospin correlations including a sign change, which is crucial to explain the experimental data.

We also note that a spin-orbital model similar to Eq. (5) was studied in Ref. 11, although the model was derived for the corner-sharing configuration of the octahedra. On the contrary, our model is derived for the edge-sharing configuration.

The orbital-lattice coupling term \mathcal{H}_{JT} in Eq. (1) is given in the form

$$\mathcal{H}_{\text{JT}} = \gamma \sum_i Q_i T_i + \frac{1}{2} \sum_i Q_i^2. \quad (13)$$

The first term describes the JT coupling where γ is the electron-lattice coupling constant and Q_i is the amplitude of the JT distortion at site i . The second term denotes the elastic energy of the JT distortion. For simplicity, we neglect the kinetic energy of phonons and regard Q_i as a classical variable. Here, we note that besides the onsite term there may be intersite interactions of JT distortions such as $\sum_{ij} Q_i Q_j$. However, in the self-consistent scheme described in Sec. IV A, which we will employ in the present numerical study, it is expected that the contribution of intersite interactions does not affect the results except for a shift of the critical temperature. Such effect can be renormalized into the γ term in Eq. (13), and therefore, we do not explicitly include the intersite term in the present Hamiltonian.

In addition to the above two terms \mathcal{H}_{so} and \mathcal{H}_{JT} defined within each 1D chain, we also consider the interchain coupling term \mathcal{H}_\perp in Eq. (1). We may consider two contributions to \mathcal{H}_\perp . One is the spin-orbital exchange interaction arising from the perturbation in the interchain transfer integrals of electrons, and the other is the interchain interaction of JT distortions. The former is expected to be negligibly small due to a rapid decay and a large anisotropy of the t_{2g} wave functions, and we therefore ignore this contribution. Instead, we take account of the latter JT contribution to the interchain coupling. The explicit form of the coupling depends on the details of the lattice structure among 1D chains, and may be very complicated. In the present study, we assume the following simple form

$$\mathcal{H}_\perp = \lambda \sum_{\langle i,j \rangle} Q_i Q_j, \quad (14)$$

where the summation is taken over the NN sites in four neighboring chains. From the lattice structure of the pyroxene compounds where the TiO_6 chains are well separated by SiO_4 tetrahedra, the coupling constant λ is expected to be small. In the following numerical calculations, we will treat the interchain JT coupling in a mean-field approximation, which is well justified for weakly-coupled 1D systems.¹⁸

Finally, we discuss the realistic values of the parameters. The σ -bond overlap integral is estimated as $t_\sigma \sim -0.3\text{eV}$ for pyroxene vanadium oxides.¹⁴ Typical estimates for Coulomb interaction parameters are $U \sim 5-6\text{eV}$ and $J_H \sim 0.6-0.7\text{eV}$.¹⁷ Hence, η in Eq. (12) is a small parameter of the order of 0.1. From the estimates of t_σ and U , the exchange energy scale J in Eq. (8) is estimated as $J \sim 200\text{K}$. As for the JT couplings γ and λ , since there is no experimental estimates to our knowledge, we treat them as parameters in the following calculations. As we will show in Sec. IV B 2, the comparison between the numerical results of the magnetic susceptibility and the experimental data gives a reasonable energy scale of the JT stabilization energy.

III. MEAN-FIELD ANALYSIS

Before going into the numerical study of the thermodynamics of the model (1), we apply a mean-field argument to capture the behavior in the ground state and in the high-temperature phase. In order to simplify the argument, we consider only the spin-orbital part \mathcal{H}_{so} in this section.

A. Ground state

In the ground state, we here consider four different types of ordered states as shown in Fig. 2 schematically; (a) the spin-ferro and orbital-ferro (sF-oF), (b) the spin-ferro and orbital-antiferro (sF-oAF), (c) the spin-antiferro and orbital-ferro, and (d) the spin-antiferro and orbital-antiferro (sAF-oAF) states. For simplicity, we consider the fully polarized states for the spin-ferro, the orbital-ferro, and the orbital-antiferro orderings, where quantum fluctuations do not play a crucial role. (Note that the orbital isospin is the Ising spin in the present model.) The important point is that as easily shown by Eqs. (6) and (7), the orbital-ferro ordering, i.e., $\langle T_i T_{i+1} \rangle = 1/4$ and $\langle T_i \rangle = 1/2$ (or $-1/2$) for all i , disconnects every other bonds. Hence, when the spin coupling is antiferromagnetic, the orbital-ferro ordering leads to the spin-singlet formation, i.e., $\langle \mathbf{S}_i \cdot \mathbf{S}_{i+1} \rangle = -3/4$ for remaining isolated NN pairs. Therefore, the ordered state (c) is denoted as the spin-dimer and orbital-ferro (sD-oF) state. We note that a similar mechanism of the singlet formation driven by orbital ordering has been proposed for a related model.¹¹

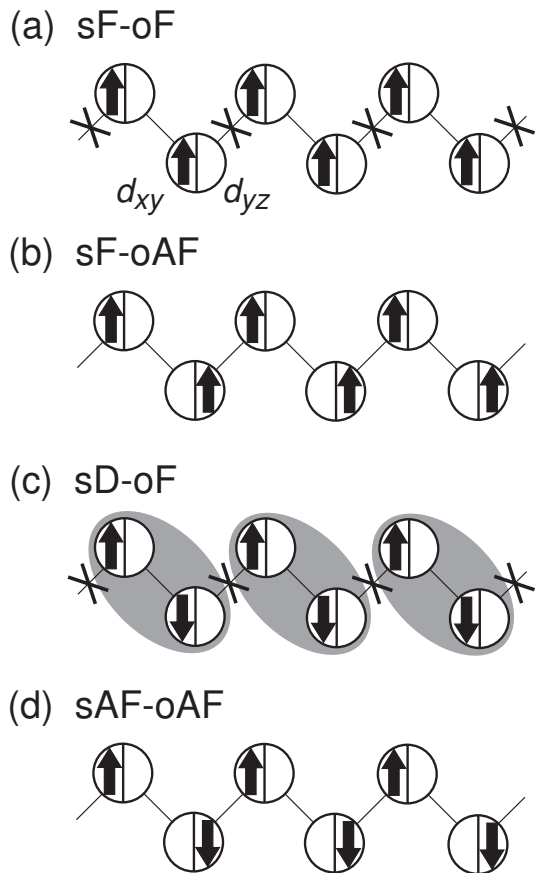


FIG. 2: Spin and orbital ordering patterns in (a) the spin-ferro and orbital-ferro (sF-oF), (b) the spin-ferro and orbital-antiferro (sF-oAF), (c) the spin-dimer and orbital-ferro (sD-oF), and (d) the spin-antiferro and orbital-antiferro (sAF-oAF) states. Circles denote the lattice sites, and two separated spaces inside them denote two different orbital states d_{xy} and d_{yz} as indicated in (a). Arrows denote spins, and gray ovals in (c) represent the spin-singlet pairs. Crosses in (a) and (c) denote the disconnected bonds by the ferro-type orbital ordering. See the text for details.

The ground-state energy for each ordered state is calculated by replacing the spin and orbital-isospin operators in Eq. (5) by the following expectation values;

$$\langle \mathbf{S}_i \cdot \mathbf{S}_{i+1} \rangle = \frac{1}{4} \quad \text{for sF pairs,} \quad (15)$$

$$\langle \mathbf{S}_i \cdot \mathbf{S}_{i+1} \rangle = -\frac{3}{4} \quad \text{for sD pairs,} \quad (16)$$

$$\langle \mathbf{S}_i \cdot \mathbf{S}_{i+1} \rangle = -s \quad \text{for sAF pairs,} \quad (17)$$

where s is a positive parameter (we do not need to specify the value of s in the following discussion), and

$$\langle T_i T_{i+1} \rangle = \frac{1}{4}, \quad \langle T_i \rangle = \pm \frac{1}{2} \quad \text{for oF pairs,} \quad (18)$$

$$\langle T_i T_{i+1} \rangle = -\frac{1}{4}, \quad \langle T_i \rangle = \pm \frac{(-1)^i}{2} \quad \text{for oAF pairs,} \quad (19)$$

respectively. The obtained ground-state energies per site

for the states (a)-(d) are

$$E_{\text{sF-oF}} = 0, \quad (20)$$

$$E_{\text{sF-oAF}} = -J \left(A + \frac{B}{4} \right), \quad (21)$$

$$E_{\text{sD-oF}} = -J \frac{C}{2}, \quad (22)$$

$$E_{\text{sAF-oAF}} = -J(A - sB), \quad (23)$$

respectively.

We compare Eqs. (20)-(23) by using Eqs. (8)-(11) for a realistic value of $\eta = J_{\text{H}}/U \sim 0.1$, and obtain

$$(E_{\text{sF-oAF}} \text{ or } E_{\text{sD-oF}}) < E_{\text{sAF-oAF}} < E_{\text{sF-oF}}. \quad (24)$$

Hence, the ground state is either (b) sF-oAF or (c) sD-oF state. From the equation of $E_{\text{sF-oAF}} = E_{\text{sD-oF}}$, we obtain the critical value of η for the transition between the two phases as

$$\eta_c = \frac{1}{3}(\sqrt{73} - 8) \simeq 0.18. \quad (25)$$

Namely, we have

$$E_{\text{sD-oF}} < E_{\text{sF-oAF}} \quad \text{for } \eta < \eta_c, \quad (26)$$

$$E_{\text{sF-oAF}} < E_{\text{sD-oF}} \quad \text{for } \eta > \eta_c. \quad (27)$$

The sD-oF (sF-oAF) phase is stable for $\eta < \eta_c$ ($\eta > \eta_c$).

The ground-state phase transition between the sD-oF and sF-oAF phases by changing η is understood by the competition between the spin superexchange interaction and the Hund's-rule coupling. The former comes from the perturbation process within the same orbitals and favors the spin-singlet state.¹⁹ The latter enhances the energy gain from the perturbation process between different orbitals and stabilizes the sF-oAF state. It is known that the sF-oAF state is always stabilized for a finite Hund's-rule coupling (finite η) in multiorbital systems with transfer integrals $t^{11} = t^{22} \neq 0$ between all the NN sites.^{20,21} In the present systems, the specific form of the transfer integrals due to the zig-zag lattice structure gives a chance to stabilize the sD-oF state in the small η regime.

From the results above, for a realistic value of $\eta \sim 0.1$, the ground state is predicted to be the sD-oF phase within the mean-field argument. This will be confirmed by the numerical calculations in Sec. IV. We will also show that the sF-oAF state is realized for larger values of η than η_c in Appendix B.

B. High-temperature para phase

At high temperatures, both spin and orbital are disordered. We here examine spin and orbital correlations in the para phase by a mean-field type argument.

First, to focus on the spin degree of freedom, we replace the orbital isospin operators in the effective model (5)

with their mean values, i.e., $T_i \rightarrow \langle T_i \rangle = 0$ and $T_i T_{i+1} \rightarrow \langle T_i T_{i+1} \rangle$. The resultant effective spin Hamiltonian reads

$$\mathcal{H}_{\text{s}}^{\text{MF}} = \sum_i (J_{i,i+1}^{\text{s}} \mathbf{S}_i \cdot \mathbf{S}_{i+1} - K_{i,i+1}^{\text{s}}), \quad (28)$$

where

$$J_{i,i+1}^{\text{s}} = J \left[\frac{1}{4}(C - 2B) + (C + 2B)\langle T_i T_{i+1} \rangle \right], \quad (29)$$

$$K_{i,i+1}^{\text{s}} = \frac{J}{4} \left[\frac{1}{4}(C + 8A) + (C - 8A)\langle T_i T_{i+1} \rangle \right]. \quad (30)$$

In the high-temperature limit, $\langle T_i T_{i+1} \rangle$ becomes zero and the effective spin exchange constant becomes

$$J_{i,i+1}^{\text{s}}(T \rightarrow \infty) = \frac{J}{4}(C - 2B), \quad (31)$$

which is positive for the realistic value of $\eta \sim 0.1$ and independent of i . Hence, we end up with a 1D AF spin Heisenberg model.

On the other hand, we can also consider a reduced Hamiltonian for the orbital degree of freedom by replacing the spin operators in the model (5) with their mean values. The result is

$$\mathcal{H}_{\text{o}}^{\text{MF}} = \sum_i [J_{i,i+1}^{\text{o}} T_i T_{i+1} - L_{i,i+1}^{\text{o}}(T_i + T_{i+1}) - K_{i,i+1}^{\text{o}}], \quad (32)$$

where

$$J_{i,i+1}^{\text{o}} = J \left[\left(2A - \frac{C}{4} \right) + (C + 2B)\langle \mathbf{S}_i \cdot \mathbf{S}_{i+1} \rangle \right], \quad (33)$$

$$L_{i,i+1}^{\text{o}} = (-1)^i J \frac{C}{2} \left(\frac{1}{4} - \langle \mathbf{S}_i \cdot \mathbf{S}_{i+1} \rangle \right), \quad (34)$$

$$K_{i,i+1}^{\text{o}} = \frac{J}{4} \left[\left(2A + \frac{C}{4} \right) - (C - 2B)\langle \mathbf{S}_i \cdot \mathbf{S}_{i+1} \rangle \right]. \quad (35)$$

In the high-temperature limit, $\langle \mathbf{S}_i \cdot \mathbf{S}_{i+1} \rangle = 0$ and the effective isospin coupling constant becomes

$$J_{i,i+1}^{\text{o}}(T \rightarrow \infty) = J \left(2A - \frac{C}{4} \right). \quad (36)$$

This coupling constant is also positive for $\eta \sim 0.1$, and therefore, we obtain a 1D antiferro-type Ising isospin model. [Note that the second term in Eq. (32) cancels out when $\langle \mathbf{S}_i \cdot \mathbf{S}_{i+1} \rangle = 0$.]

The above arguments indicate that both spin and orbital correlations are antiferro type in the high-temperature limit in our effective model. On the contrary, as discussed in Sec. III A, the ground state is either the sF-oAF or sD-oF states. This suggests that either spin or orbital correlation has to change from antiferro to ferro type as decreasing temperature. The expression for the effective spin coupling constant $J_{i,i+1}^{\text{s}}$ in Eq. (29)

implies that development of antiferro-type orbital correlations $\langle T_i T_{i+1} \rangle < 0$ may change the sign of $J_{i,i+1}^s$ from positive (antiferro) to negative (ferro). In a similar way, Eq. (33) suggests that development of AF spin correlations $\langle \mathbf{S}_i \cdot \mathbf{S}_{i+1} \rangle < 0$ may induce the sign change of $J_{i,i+1}^o$. In this manner, the spin and orbital correlations compete with each other. Within the mean-field-level argument, it is highly nontrivial whether the spin or orbital correlation changes the sign as temperature decreases, and how the sign change takes place by the competition. In the next section, we will show by numerical calculations that this nontrivial sign change indeed occurs owing to the interplay between spin and orbital degrees of freedom.

IV. NUMERICAL ANALYSIS

A. Method

To study thermodynamic properties of the model (1), we apply the quantum transfer matrix (QTM) method²² combined with the mean-field treatment of the JT distortions. Here, we describe the scheme of our analysis.

Since the present model (1) is highly 1D anisotropic, it is justified to treat the small interchain coupling in the mean-field approximation and to solve an effective 1D model.¹⁸ Hence, in the following numerical analysis, we determine the JT distortions self-consistently as described below by including the interchain coupling as the mean field in the form

$$\tilde{\mathcal{H}}_{\perp} = \lambda \sum_{\langle i,j \rangle} Q_i \tilde{Q}_j = -z|\lambda| \sum_i Q_i^2, \quad (37)$$

where \tilde{Q}_j is the mean-field value of the JT distortion at site j and z is the number of NN chains, i.e., $z = 4$ in the present materials. As a result, the total Hamiltonian, $\mathcal{H}_{\text{so}} + \mathcal{H}_{\text{JT}} + \tilde{\mathcal{H}}_{\perp}$, is reduced to an effective 1D spin-orbital-lattice coupled model in the form

$$\begin{aligned} \tilde{\mathcal{H}} &= \mathcal{H}_{\text{so}} + \gamma \sum_i Q_i T_i + \frac{1-2z|\lambda|}{2} \sum_i Q_i^2 \\ &= \mathcal{H}_{\text{so}} + \bar{\gamma} \sum_i \bar{Q}_i T_i + \frac{1}{2} \sum_i \bar{Q}_i^2, \end{aligned} \quad (38)$$

where the JT coupling and distortion are rescaled as $\bar{\gamma} = \gamma/\sqrt{1-2z|\lambda|}$ and $\bar{Q}_i = \sqrt{1-2z|\lambda|}Q_i$, respectively. For later use, we define the JT stabilization energy as

$$\Delta_{\text{JT}} = \bar{\gamma}^2/8, \quad (39)$$

which is the energy gain by the JT distortion in the case of $J = 0$ in \mathcal{H}_{so} .

The optimal values of the JT distortions $\{\bar{Q}_i\}$ are determined in a self-consistent way. We start from an initial guess of $\{Q_i\}$ and calculate the expectation values of the isospin $\langle T_i \rangle$ by applying the QTM method to the effective 1D model $\tilde{\mathcal{H}}$. Note that the QTM calculation is numerically exact and includes all the fluctuations in spin and

orbital degrees of freedom within the 1D chain for a given set of $\{\bar{Q}_i\}$. See Appendix A for the details of the QTM method. The obtained values of $\langle T_i \rangle$ are used to determine $\{\bar{Q}_i\}$ self-consistently. The self-consistent equation is obtained by the energy minimization $\delta\langle \mathcal{H} \rangle / \delta \bar{Q}_i = 0$ which gives

$$\bar{Q}_i^{\text{new}} = -\bar{\gamma} \langle T_i \rangle. \quad (40)$$

The values of $\{\bar{Q}_i^{\text{new}}\}$ are used as inputs for the next QTM calculation. We iterate the procedure until $\{\bar{Q}_i\}$ converge to optimal values.

For the optimal values of $\{\bar{Q}_i\}$, we evaluate thermodynamic quantities of the system by the QTM method. We calculate the magnetization per site,

$$m = \frac{1}{L} \sum_i \langle S_i^z \rangle, \quad (41)$$

and the average values of NN spin and orbital correlations,

$$C_s = \frac{1}{L} \sum_i \langle \mathbf{S}_i \cdot \mathbf{S}_{i+1} \rangle, \quad (42)$$

$$C_o = \frac{1}{L} \sum_i \langle T_i T_{i+1} \rangle, \quad (43)$$

respectively, where L is the length of the chain. We also define the NN spin correlations on odd and even bonds as

$$C_s^{\text{odd}} = \frac{2}{L} \sum_{i \in \text{odd}} \langle \mathbf{S}_i \cdot \mathbf{S}_{i+1} \rangle, \quad (44)$$

$$C_s^{\text{even}} = \frac{2}{L} \sum_{i \in \text{even}} \langle \mathbf{S}_i \cdot \mathbf{S}_{i+1} \rangle, \quad (45)$$

respectively, to detect the spin dimerization. See Eqs. (A6)-(A10) in Appendix A for the calculation of these quantities. Besides, we calculate the magnetic susceptibility χ by taking the derivative of m to the external magnetic field. We perform the calculation within the same framework for the system under the external magnetic field whose Hamiltonian reads

$$\tilde{\mathcal{H}} - g\mu_B H \sum_i S_i^z, \quad (46)$$

where g is the g -factor and μ_B is the Bohr magneton, and H is the external magnetic field. The susceptibility is obtained from the numerical derivative of m as

$$\chi = \frac{m(\Delta H) - m(0)}{\Delta H}, \quad (47)$$

where we use $\Delta H = 0.001J/(g\mu_B)$.

The QTM method allows us to treat the system in the thermodynamic limit directly (see Appendix A). Namely, we can obtain the results in the limit of $L \rightarrow \infty$ without finite-size effects. On the other hand, the results contain

a systematic error due to a finite Trotter number M . We need to check carefully the convergence of the results with increasing M . The values of M used in the following calculations are up to $M = 4$ for the case of $\bar{\gamma} = 0$ while up to $M = 3$ for $\bar{\gamma} > 0$. Although these values of M appear to be rather small, we will show that the M -convergence is excellent for the temperature range in the present study, $T \gtrsim 0.1J$.

B. Results

In this section, we show our numerical results for thermodynamic properties of the model (1) obtained by the method in the previous section.

In Sec. IV B 1, we examine the interplay between orbital and spin degrees of freedom in the absence of the JT coupling. For realistic small values of $\eta \sim 0.1$, we find that the system exhibits the sD-oF ground state as predicted in the mean-field argument in Sec. III A, and there occurs a nontrivial feedback effect between orbital and spin at finite temperatures. For larger values of η , the system shows the phase transition to the sF-oAF state, and the behavior in this regime will be discussed in Appendix B.

In Sec. IV B 2, we switch on the JT coupling which causes a finite-temperature transition. We compare our numerical results of the magnetic susceptibility with the experimental data for $\text{NaTiSi}_2\text{O}_6$. We estimate the parameters in our model from the comparison, and conclude that our model with realistic parameters captures the essential physics of the pyroxene compounds. We also show temperature dependences of the spin and orbital correlations and the magnitude of the spin dimerization.

1. Interplay between orbital and spin

In order to explore the interplay between orbital and spin degrees of freedom, we first show our results in the absence of the JT coupling ($\bar{\gamma} = 0$). In this case, the model is reduced to the 1D spin-orbital model \mathcal{H}_{so} [Eq. (5)], and we can obtain thermodynamic properties by performing the QTM calculation without any self-consistent iteration.

Figure 3 shows the results of the magnetic susceptibility χ in Eq. (47) for several values of η . Note that the results for different values of the Trotter number $M = 2, 3$, and 4 almost coincide with each other as shown in the figure, which ensures the convergence of the QTM results in this parameter range. The magnetic susceptibility increases as decreasing temperature, and exhibits a broad peak at some temperature. At a lower temperature, it decays rapidly and approaches zero as $T \rightarrow 0$. While the peak becomes sharper and shifts to a lower temperature region as η increases, the rapid decay of χ at low temperatures is commonly observed for the values of η plotted in the figure. This indicates that our spin-orbital

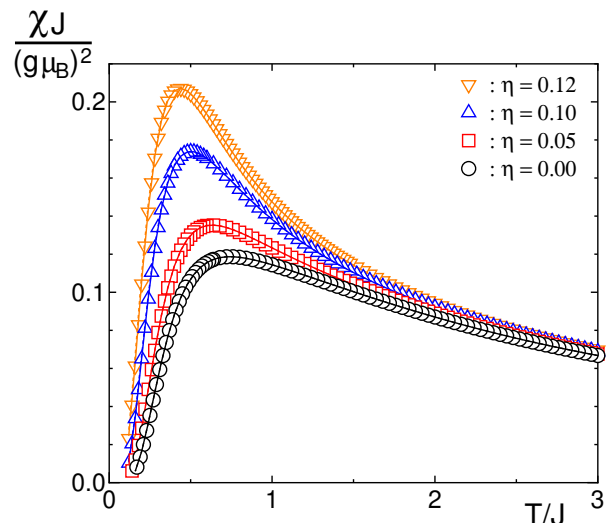


FIG. 3: Temperature dependence of the magnetic susceptibility χ for $\eta = 0.0, 0.05, 0.10$, and 0.12 . Symbols represent the results for $M = 4$ while solid and dotted curves are those for $M = 3$ and $M = 2$, respectively.

model \mathcal{H}_{so} in Eq. (5) with a realistic value of $\eta \sim 0.1$ exhibits the spin-singlet ground state as predicted in the mean-field-type argument in Sec. III A.

To clarify the nature of the system in more detail, in Fig. 4, we show the results of NN spin and orbital correlations C_s and C_o defined in Eqs. (42) and (43), respectively. The M -dependence of the results is negligible also in this case. We note that at finite temperatures no true long-range order appears in the 1D spin-orbital model \mathcal{H}_{so} , and the NN spin correlations are uniform, i.e., $C_s = C_s^{\text{odd}} = C_s^{\text{even}}$. As $T \rightarrow 0$, the spin and orbital correlations converge to $C_s = -3/8$ and $C_o = 1/4$, respectively, which are the values expected in the sD-oF ground state shown in Fig. 2 (c). (Note that in the sD-oF ground state, $\langle \mathbf{S}_i \cdot \mathbf{S}_{i+1} \rangle$ takes the value of $-3/4$ or 0 alternatively from bond to bond, while $\langle T_i^z T_{i+1}^z \rangle = 1/4$ for all bonds.) Hence, we conclude that the ground state of the system is the sD-oF state in Fig. 2 (c) for the realistic values of $\eta \sim 0.1$, and the rapid decay of χ at low temperatures in Fig. 3 is due to the spin-singlet formation in the dimerized pairs.

Let us examine the finite-temperature behavior of C_s and C_o in Fig. 4. At high temperatures, both the spin and orbital correlations are negative, i.e., antiferro type, being consistent with the mean-field prediction in Sec. III B. Here, the spin and orbital antiferro correlations compete with each other since the spin-antiferro correlation favors the orbital-ferro one and vice versa as indicated in the form of \mathcal{H}_{so} in Eq. (5). We find that in this range of η the spin-antiferro correlation grows more rapidly than the orbital correlation as T decreases. This growth of C_s suppresses C_o and causes the sign change of C_o from antiferro to ferro type. Once C_o becomes ferro type, C_s and C_o develop cooperatively, and eventually the ferro-

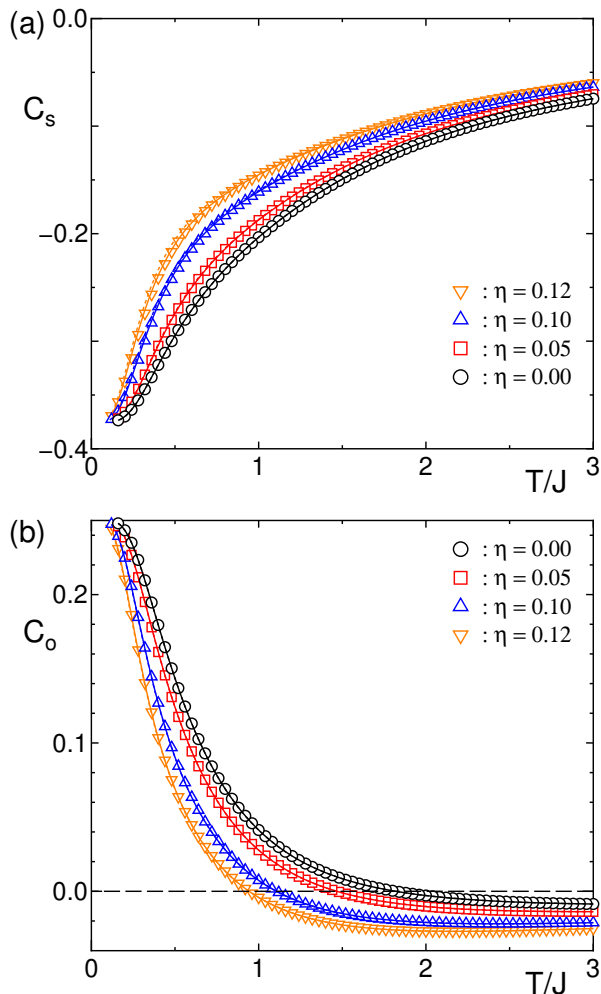


FIG. 4: Temperature dependences of (a) the nearest-neighbor spin correlation C_s and (b) the nearest-neighbor orbital correlation C_o for $\eta = 0.0, 0.05, 0.10$, and 0.12 . Symbols represent the results for $M = 4$ while solid and dotted curves are those for $M = 3$ and $M = 2$, respectively.

type orbital correlation induces the spin-dimer formation. These results clearly indicate that our model \mathcal{H}_{so} shows a nontrivial feedback effect between orbital and spin degrees of freedom at finite temperatures.

The strong interplay between orbital and spin also shows up in the temperature dependence of the magnetic susceptibility at high temperatures. There, we expect a deviation from the Curie-Weiss behavior due to the interplay. The deviation can be monitored by the temperature dependence of the effective spin exchange coupling $J_{i,i+1}^s$ in Eq. (29), since it corresponds to an effective Curie-Weiss temperature Θ_{CW} . (In the mean-field approximation, $\Theta_{\text{CW}} = J_{i,i+1}^s$ in the 1D spin-1/2 system with NN interaction.) As mentioned in Sec. III B, the effective spin exchange coupling $J_{i,i+1}^s$ depends on the NN orbital correlation $\langle T_i T_{i+1} \rangle$.

In Fig. 5, we show the temperature dependence of the

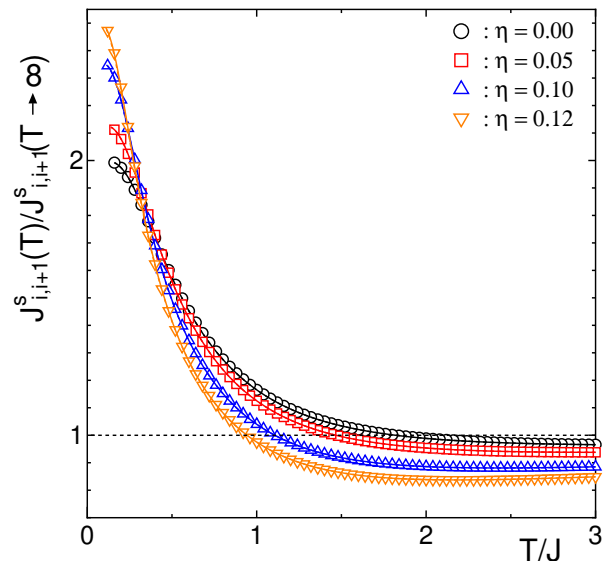


FIG. 5: Effective spin exchange coupling $J_{i,i+1}^s$ in Eq. (29) for $\eta = 0.0, 0.05, 0.10$, and 0.12 . The results are scaled by their values at high-temperature limit, $J_{i,i+1}^s(T \rightarrow \infty)$.

effective spin exchange coupling $J_{i,i+1}^s$ in Eq. (29) scaled by the value in the high-temperature limit. The results clearly show that the effective spin exchange coupling is temperature-dependent even in the temperature range where the Curie-Weiss fitting to the experimental data has been attempted in Ref. 8. (The energy scale of J will be estimated as 200 – 300K from the fitting in the next section.) This suggests that the temperature dependence of χ in the present system deviates from the Curie-Weiss law in the experimental temperature range. We need further careful considerations in the fitting of the experimental data of the magnetic susceptibility to estimate the model parameters.

2. Comparison with experimental results

Next, to compare our numerical results with experimental data quantitatively, we show our results in the presence of the JT coupling, i.e., for the case of $\bar{\gamma} > 0$ in Eq. (38). For a finite $\bar{\gamma}$, our model with $\eta \sim 0.1$ exhibits a finite-temperature transition from the high-temperature para phase to the low-temperature sD-oF phase, and the magnetic susceptibility shows a rapid decay below the critical temperature as observed in experiment. Here, we perform the numerical fitting of our results to the experimental data. The numerical results shown in the following are obtained from the self-consistent iteration of the QTM calculation with $M = 3$, and we have confirmed the M -convergence of the results.

Figure 6 shows the comparison between our numerical results and the experimental data of the magnetic susceptibility χ . We plot the numerical results for several

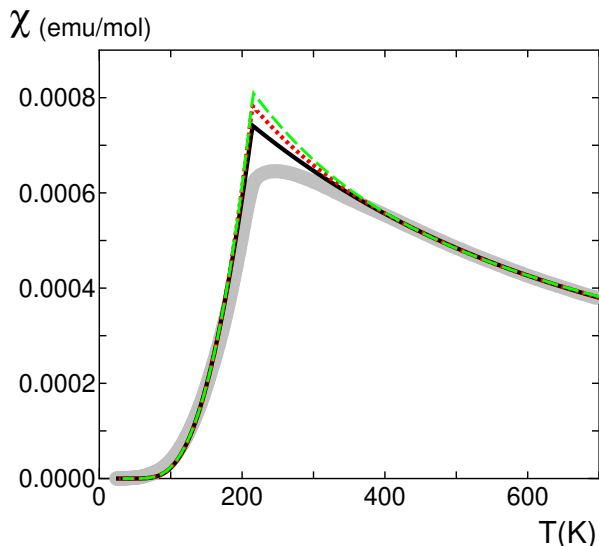


FIG. 6: Comparison between numerical and experimental results of the magnetic susceptibility χ . Solid, dotted, and dashed curves represent the numerical results for $(J, \eta, g, \Delta_{\text{JT}}) = (213\text{K}, 0.05, 1.85, 86\text{K})$, $(250\text{K}, 0.10, 1.87, 90\text{K})$, and $(296\text{K}, 0.12, 1.90, 89\text{K})$, respectively. Bold gray curve represents the experimental data in Ref. 8.

typical parameter sets given by the fitting procedure explained below. As for the experimental data, we plot the results for $\text{NaTiSi}_2\text{O}_6$. The data correspond to χ_m in Ref. 8 which contain only the intrinsic contributions after the subtractions of a Curie contribution from magnetic impurities and a constant term due to core-electron diamagnetism and the Van Vleck paramagnetism. The experimental data increase as T decreases at high temperatures, and exhibit a sharp drop at $T_c = 210\text{K}$.

The numerical fitting is performed in the following way. In our model, there are four parameters, i.e., the effective exchange coupling J , the ratio of Coulomb interactions $\eta = J_{\text{H}}/U$, the g -factor g , and the JT coupling parameter $\bar{\gamma}$. First, we choose a certain value of η . Then, we estimate the optimal values of J and g from the least-square fitting of the numerical results to the experimental data in a high-temperature regime of $400\text{K} < T < 700\text{K}$. We note that the susceptibility in the high-temperature regime is not affected by the JT coupling $\bar{\gamma}$ in the present scheme of the calculation. Using the estimates of J and g , we determine the value of $\bar{\gamma}$ to reproduce the critical temperature $T_c = 210\text{K}$. We thereby obtain the optimal set of J , g , and $\bar{\gamma}$ for a certain value of η . By changing the value of η in the reasonable range, we obtained the estimates of the four parameters in our model.

In Fig. 6, we show the results of the fitting for $\eta = 0.05, 0.10$, and 0.12 as typical examples. As shown in the figure, the numerical results well reproduce the experimental data except for the narrow temperature range close to T_c . We consider that the small deviation near T_c is the artifact of the approximation in the treatment

of the JT distortion \bar{Q}_i : Our method to determine \bar{Q}_i in the self-consistent calculation is not able to include the short-range correlations and thermal fluctuations of lattice distortions, which are critically enhanced close to T_c . The short-range correlations and critical fluctuations induce the spin-singlet fluctuation, and therefore, they suppress the magnetic susceptibility χ in the critical region. We believe that when such effects are taken into account in an appropriate way, the agreement between the numerical results and the experimental data becomes better near T_c . This interesting problem is left for further study. Hence, it is reasonable that our method overestimates χ close to the critical point, where the effects of the short-range correlations and fluctuations becomes significant. Therefore, we consider that the agreement of the fitting results with the experimental data is satisfactorily good within the present scheme of the calculation.

From the fitting, we obtained the estimates of the parameters as $(J = 213\text{K}, g = 1.85, \Delta_{\text{JT}} = 86\text{K})$ for $\eta = 0.05$, $(J = 250\text{K}, g = 1.87, \Delta_{\text{JT}} = 90\text{K})$ for $\eta = 0.10$, and $(J = 296\text{K}, g = 1.90, \Delta_{\text{JT}} = 89\text{K})$ for $\eta = 0.12$, where $\Delta_{\text{JT}} = \bar{\gamma}^2/8$ as defined in Eq. (39). Although we cannot determine the best set of the values only from the present fitting, we find that the estimates are quite reasonable in this t_{2g} compound: The estimates of $J \sim 200 - 300\text{K}$ are comparable to the estimate based on microscopic parameters in Sec. II. As for the g -factor, although there is no definite estimate for the present compound as far as we know, it is known that g becomes smaller than two in many t_{2g} compounds such as titanates and vanadates. For instance, it has been reported that $g \sim 1.9 - 2$ for TiOCl (Ref. 23) and for NaV_2O_5 .²⁴ Hence, we believe that our estimates of g are reasonable. Furthermore, the estimates of $\Delta_{\text{JT}} \sim 90\text{K}$, which are smaller than the exchange energy J , also appear to be reasonable for t_{2g} electron systems. (We will comment on the magnitude of Δ_{JT} in the end of this section.) Therefore, we believe that our effective model (1) with realistic parameters can describe successfully the peculiar properties of the pyroxene compound $\text{NaTiSi}_2\text{O}_6$.

As shown in Fig. 6, the magnetic susceptibility of our model shows an exponential decay at low temperatures well below T_c . We estimate the spin gap Δ_s from the results below $0.5T_c$ by the fitting function

$$\chi \propto \exp(-\Delta_s/T). \quad (48)$$

The estimates of Δ_s are 665, 640, and 638K for $\eta = 0.05, 0.10$, and 0.12 , respectively. In experiment, the spin gap Δ_s is estimated as $\sim 500\text{K}$,⁸ which is comparable to our numerical results.

Next, for these realistic parameters, we examine the spin and orbital correlations. Figure 7 shows the temperature dependences of the NN spin correlations C_s , C_s^{odd} , and C_s^{even} , and the NN orbital correlation C_o . Here, we show only the results for the parameter set of $(J, \eta, \Delta_{\text{JT}}) = (250\text{K}, 0.10, 90\text{K})$ as a typical example since essentially the same behavior is obtained for other parameter sets in Fig. 6.²⁵ The correlations take the same values

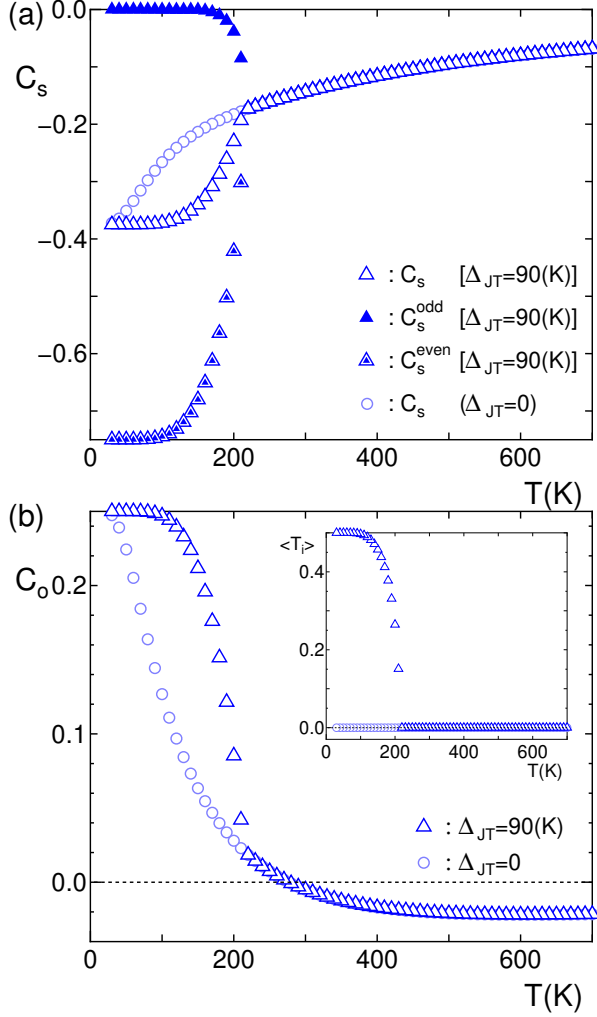


FIG. 7: Temperature dependences of (a) the nearest-neighbor spin correlations C_s , C_s^{odd} , and C_s^{even} , and (b) the nearest-neighbor orbital correlation C_o for $(J, \eta, \Delta_{JT}) = (250\text{K}, 0.10, 90\text{K})$. Circles show the data for $\Delta_{JT} = 0$ for comparison. Inset in (b): Polarization of orbital isospin.

as those for $\Delta_{JT} = 0$ at high temperatures, and start to deviate at the transition temperature $T_c = 210\text{K}$. Below T_c , the NN spin correlations on odd and even bonds, C_s^{odd} and C_s^{even} , take different values and converge to $-3/4$ or 0 as $T \rightarrow 0$. (Note that in the low-temperature ordered phase, one of the doubly-degenerate ordered states is selected depending on the initial set of $\{\bar{Q}_i\}$ used in the self-consistent calculation.) This indicates that the translational symmetry is broken in the spin-dimer phase. On the other hand, the NN orbital correlation C_o is uniform, and goes to the value of $1/4$ as $T \rightarrow 0$. As shown in the inset of Fig. 7 (b), the isospin polarization $\langle T_i \rangle$ becomes finite below T_c , indicating the long-range orbital ordering. These results explicitly show that the system at low temperatures is in the sD-oF phase in Fig. 2 (c).

In Fig. 8, we plot the effective spin exchange coupling $J_{i,i+1}^s$, corresponding to Eq. (29) in the case of $\Delta_{JT} = 0$.

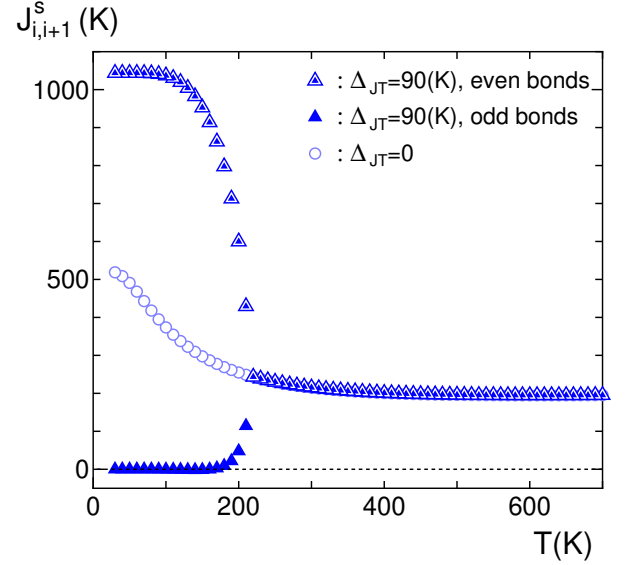


FIG. 8: Temperature dependence of the effective spin exchange coupling $J_{i,i+1}^s$ [Eq. (49)] for $(J, \eta, \Delta_{JT}) = (250\text{K}, 0.10, 90\text{K})$. Circles show the data for $\Delta_{JT} = 0$ for comparison.

In the case of a finite Δ_{JT} , we have to keep the linear terms of $\langle T_i \rangle$ in the reduced spin Hamiltonian in Eq. (28). The resultant expression for the effective spin exchange coupling is

$$J_{i,i+1}^s = J \left[\frac{1}{4}(C - 2B) + (C + 2B)\langle T_i T_{i+1} \rangle - \frac{(-1)^i C}{2} (\langle T_i \rangle + \langle T_j \rangle) \right], \quad (49)$$

instead of Eq. (29). The value of $J_{i,i+1}^s$ deviates from that for $\Delta_{JT} = 0$ below T_c , and takes two alternative values from bond to bond. This clearly shows the alternating behavior of the magnetic coupling in the spin-dimer state. At low temperatures below $\sim 150\text{K}$, the dimerization is almost perfect, i.e., $J_{i,i+1}^s$ on the weak bonds is almost zero. Hence, there the system consists of almost independent spin-singlet pairs. Note that $J_{i,i+1}^s$ on the strong bonds is surprisingly enhanced up to $\sim 1000\text{K}$. The almost perfect dimerization and the enhanced exchange coupling are the unique aspects of the present spin-orbital-lattice coupled system.

Our estimates of the JT stabilization energy $\Delta_{JT} \sim 90\text{K}$ are considerably smaller than $T_c = 210\text{K}$ as well as $J = 200 - 300\text{K}$. This suggests that the critical temperature T_c is not determined mainly by the JT coupling, and that the balance of the JT coupling and the spin-orbital intersite interaction is important in this t_{2g} electron system. Moreover, we note that the phase transition occurs below the temperature where the orbital correlation C_o changes its sign from negative (antiferro type) to positive (ferro type) as shown in Fig. 7 (b). This indicates an importance of the interplay and the feedback effect be-

tween spin and orbital in the present system. Therefore, we consider that the pyroxene compounds are typical t_{2g} electron systems where the JT energy scale is relatively small and the bare interplay between spin and orbital degrees of freedom plays a central role in the thermodynamic properties.

V. SUMMARY AND CONCLUDING REMARKS

In this paper, we have studied the effective spin-orbital-lattice coupled model which we derived to understand the peculiar phase transition to the spin-singlet state in $ATiSi_2O_6$ ($A = Na, Li$). Using the mean-field-type analysis and the numerical quantum transfer matrix method, we have clarified that the interplay between spin and orbital degrees of freedom plays a central role in thermodynamic properties of the system. At high temperatures, both spin and orbital correlations are antiferro type and compete with each other. As temperature decreases, the antiferromagnetic spin correlation grows rapidly and yields the sign change of the orbital correlation from antiferro to ferro type so that the frustration is released. This ferro-type orbital correlation with the Jahn-Teller coupling finally causes a transition to the spin-dimer and orbital-ferro ordered phase. This feedback effect between orbital and spin degrees of freedom results in peculiar temperature dependence of the magnetic susceptibility. We have shown that the magnetic susceptibility data for $NaTiSi_2O_6$ can be explained by our effective model with realistic values of parameters.

The transition to the spin-singlet state in the present system shows several different aspects from conventional spin-Peierls systems. One is the temperature dependence of the magnetic susceptibility. In the present system, the rapid decay of the susceptibility due to the spin-singlet formation occurs even without a broad peak as a fingerprint of well-developed spin correlations. This is because the driving force of the transition is not the magnetoelastic interaction but the orbital-ferro correlations assisted by the Jahn-Teller distortion. However, this does not mean that the orbital-lattice physics is dominant as in e_g electron systems such as CMR manganites. In the present t_{2g} electron system, the Jahn-Teller energy scale is considerably smaller than the orbital and spin exchange interactions, and the orbital-ferro correlation is induced by the keen competition between the orbital and spin degrees of freedom. These illuminate a unique feature of the present t_{2g} system, namely, there the interplay between orbital and spin appears explicitly without being dominated by Jahn-Teller physics.

Another peculiar aspect of the spin-dimer state in our model is that the spin-singlet pairs are formed on the longer Ti-Ti bonds rather than the shorter ones. In the present system, say, the d_{xy} orbital ordering is concomitant with the flattening of TiO_6 octahedra in the z direction which elongates Ti-Ti bonds in the xy plane. Since the spin exchange interaction is strong between

the nearest-neighbor sites in the xy plane in this d_{xy} ordered state, the spin-singlet dimers are formed on the longer Ti-Ti bonds. This aspect is clearly different from the conventional spin-Peierls systems in which the spin-singlet pairs are on shorter bonds. In our model, however, we take account of only the tetragonal Jahn-Teller mode which couples with d_{xy} and d_{yz} orbitals. For detailed comparisons with the experimental data which show much complicated lattice structure at low temperatures, it is necessary to include more general lattice distortions in our theory. In particular, we note that the magnetoelastic coupling can be substantial in the low-temperature orbital-ordered phase since the orbital-ferro ordering largely enhances the effective spin exchange coupling on strong bonds up to $\sim 1000K$ as shown in Sec. IV B 2. The magnetoelastic coupling will cause an opposite effect on the Ti-Ti bond lengths since it tends to shorten the spin-singlet Ti-Ti bonds. Further study is necessary to conclude the low-temperature lattice structure. Note that the inclusion of such magnetoelastic effect does not alter our conclusions on the mechanism of the phase transition because it becomes important only when the orbital-ferro ordering is well established far below the critical temperature.

In the present study, we have compared our results of the magnetic susceptibility with the experimental data for the Na compound $NaTiSi_2O_6$. There is another compound in this pyroxene family, i.e., $LiTiSi_2O_6$. The Li compound also shows the phase transition at $T_c = 230K$ showing a sudden decay of the magnetic susceptibility below T_c .⁸ However, the susceptibility data show some extra anomalies probably due to impurity phases. We believe that our model describes essential physics in both the Na and Li compounds. Further experimental study including the sample preparation is desired to compare the data of Li compounds to our results in more detail.

As shown in Sec. III A and in Appendix B, the low-temperature phase of our effective model turns into the spin-ferro and orbital-antiferro ordered state for larger values of η than the critical value of $\eta_c \simeq 0.18$. The parameter η is the ratio of the Hund's-rule coupling to the intraorbital Coulomb repulsion, and is considered to be $\eta \sim 0.1 < \eta_c$ in the present compounds. Unfortunately, it is difficult to control the parameter η experimentally, however, it may vary for different compounds to some extent. If η becomes close to η_c in some compound, there would occur interesting phenomena related to the criticality of the phase transition at η_c . One interesting example is the phase transition from the spin-dimer and orbital-ferro state to the spin-ferro and orbital-antiferro state by applying the external magnetic field. We have investigated this issue in our effective model, and indeed observed the field-induced phase transition. The results will be reported elsewhere. The experimental study of this issue is left for future study.

Acknowledgments

We would like to thank M. Isobe for useful discussions and providing us the experimental data. We also appreciate H. Seo for valuable comments and drawing our attention to the present problem in the early stage of the study. This work is supported by NAREGI Nanoscience Project.

APPENDIX A: QUANTUM TRANSFER MATRIX METHOD

In this appendix, we briefly review the algorithm of the QTM method.²² The QTM calculation is applied to the effective 1D model (38) in the self-consistent scheme as described in Sec. IV A.

After the Suzuki-Trotter decomposition, the partition function is represented in terms of the transfer matrix as

$$Z = \text{Tr} e^{-\beta\tilde{\mathcal{H}}} = \lim_{M \rightarrow \infty} \text{Tr} \prod_{n=1}^{L/2} \mathcal{T}_M \quad (\text{A1})$$

where $\beta = 1/T$ (we set the Boltzmann constant $k_B = 1$), M is the Trotter number, and L is the system size. The transfer matrix \mathcal{T}_M is given by

$$\mathcal{T}_M = \left[e^{-\beta\tilde{h}_{2n-1,2n}/M} e^{-\beta\tilde{h}_{2n,2n+1}/M} \right]^M, \quad (\text{A2})$$

where $\tilde{\mathcal{H}}$ is decomposed into the summation of the local Hamiltonian $\tilde{h}_{i,i+1}$ for bond $(i, i+1)$. We omitted the index n on the transfer matrix \mathcal{T}_M since \mathcal{T}_M for the present system is invariant under the two-site translation.

The advantage of the QTM method is that we can calculate thermodynamic quantities directly from the largest eigenvalue λ_{\max} and the corresponding right $|v^r\rangle$ and left $\langle v^l|$ eigenvectors of \mathcal{T}_M .²⁶ (Note that the eigenvectors $|v^r\rangle$ and $\langle v^l|$ are different in general since \mathcal{T}_M is an asymmetric matrix.) The partition function of the infinite system is found to be $Z = \lim_{L \rightarrow \infty} \lambda_{\max}^{L/2}$, and consequently, the free energy per site can be obtained as

$$f = -\frac{1}{2\beta} \ln \lambda_{\max}. \quad (\text{A3})$$

Hence, once the value of λ_{\max} is obtained, we can calculate any bulk quantity in the thermodynamic limit by taking the appropriate derivative of the free energy f .

Furthermore, we can calculate expectation values of site and bond operators.²⁷ For instance, an expectation value of a product of operators $\mathcal{O}_{2n-1,2n}\mathcal{O}_{2n,2n+1}$ defined at sites $(2n-1, 2n, 2n+1)$ is obtained from the formula

$$\langle \mathcal{O}_{2n-1,2n}\mathcal{O}_{2n,2n+1} \rangle = \lim_{M \rightarrow \infty} \frac{\langle v^l | \mathcal{T}_M^{\mathcal{O}} | v^r \rangle}{\lambda_{\max}}, \quad (\text{A4})$$

where

$$\begin{aligned} \mathcal{T}_M^{\mathcal{O}} &= \mathcal{O}_{2n-1,2n}\mathcal{O}_{2n,2n+1} \\ &\times \left[e^{-\beta\tilde{h}_{2n-1,2n}/M} e^{-\beta\tilde{h}_{2n,2n+1}/M} \right]^M. \end{aligned} \quad (\text{A5})$$

In the present study, we diagonalize the transfer matrix \mathcal{T}_M numerically using the simple power method, which is known to be stable for the diagonalization of asymmetric matrix.²⁸ Then, using Eqs. (A4) and (A5), we calculate the magnetization m [Eq. (41)] and the NN spin and orbital correlations C_s and C_o [Eqs. (42) and (43)], given by

$$m = \frac{\langle S_{2n-1}^z \rangle + \langle S_{2n}^z \rangle}{2}, \quad (\text{A6})$$

$$C_s = \frac{\langle \mathbf{S}_{2n-1} \cdot \mathbf{S}_{2n} \rangle + \langle \mathbf{S}_{2n} \cdot \mathbf{S}_{2n+1} \rangle}{2}, \quad (\text{A7})$$

$$C_o = \frac{\langle T_{2n-1}T_{2n} \rangle + \langle T_{2n}T_{2n+1} \rangle}{2}, \quad (\text{A8})$$

respectively. The NN spin correlations on odd and even bonds [Eqs. (44) and (45)] are given by

$$C_s^{\text{odd}} = \langle \mathbf{S}_{2n-1} \cdot \mathbf{S}_{2n} \rangle, \quad (\text{A9})$$

$$C_s^{\text{even}} = \langle \mathbf{S}_{2n} \cdot \mathbf{S}_{2n+1} \rangle, \quad (\text{A10})$$

respectively. In the spin-dimer phase, C_s^{odd} and C_s^{even} may take different values.

APPENDIX B: TRANSITION TO SPIN-F AND ORBITAL-AF PHASE

In this appendix, we discuss thermodynamic properties of the model (1) for larger values of η than those studied in Sec. IV B. There, the sF-oAF ground state is expected to be stable from the mean-field-type analysis in Sec. III A.

We first discuss our numerical results for the spin-orbital model \mathcal{H}_{so} , i.e., the effective model (38) without the JT coupling $\tilde{\gamma} = 0$. Figure 9 (a) shows the results of the magnetic susceptibility χ . The result for $\eta = 0.16$ exhibits a sharp drop as $T \rightarrow 0$, indicating the spin-singlet ground state. This behavior is similar to the results in Fig. 3. On the contrary, for $\eta = 0.18$ and 0.20 , χ exhibits a divergent behavior as $T \rightarrow 0$, suggesting that the ground state is magnetic. These suggest that there is a ground-state phase transition between nonmagnetic and magnetic phases at $\eta = \eta_c \sim 0.18$.

To clarify the nature of the transition in more detail, we show the results of NN spin and orbital correlations C_s and C_o in Figs. 9 (b) and (c), respectively. (Note that $C_s^{\text{odd}} = C_s^{\text{even}} = C_s$ for $\tilde{\gamma} = 0$ and $T > 0$.) For $\eta = 0.16$, the AF spin correlation grows rapidly as temperature decreases, resulting in the sign change of the orbital correlation from antiferro to ferro type. Then, in the limit of $T \rightarrow 0$, they approach the values of $C_s = -3/8$ and $C_o = 1/4$. These features are similar to those for smaller η shown in Sec. IV B, and indicate that the system exhibits the sD-oF ground state. For $\eta = 0.20$, on the other hand, the antiferro-type orbital correlation C_o develops rapidly, yielding the sign change of the spin correlation C_s . After the sign change, the two correlations grow cooperatively, and approach the values of $C_s = 1/4$ and

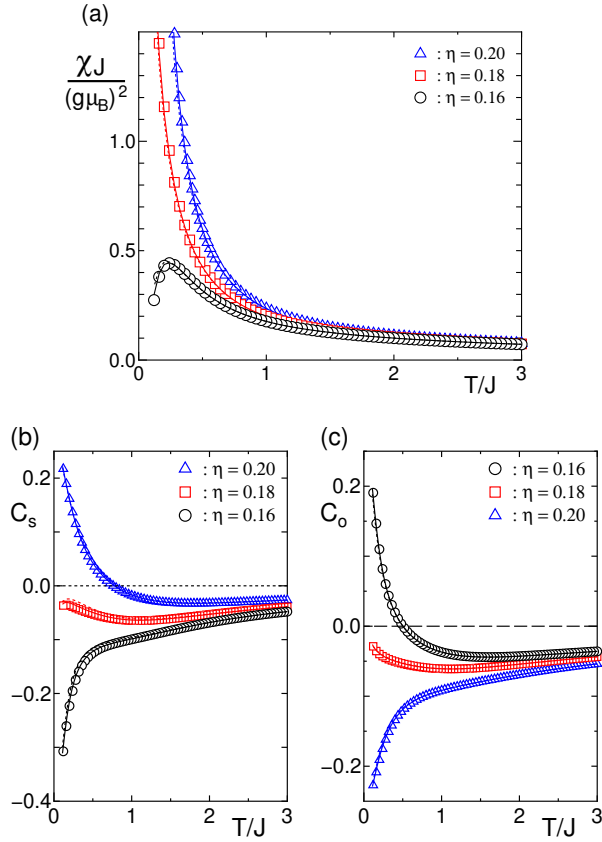


FIG. 9: Temperature dependences of (a) the magnetic susceptibility χ , (b) the nearest-neighbor spin correlation C_s , and (c) the nearest-neighbor orbital correlation C_o for $\eta = 0.16, 0.18$ and 0.20 . Symbols represent the results for $M = 4$ while solid and dotted curves are those for $M = 3$ and $M = 2$, respectively.

$C_o = -1/4$ as $T \rightarrow 0$. These are the values expected in the sF-oAF ground state shown in Fig. 2 (b). Hence, the system with $\eta = 0.20$ exhibits the sF-oAF ground state. For $\eta = 0.18$, C_s and C_o are both antiferro type and compete with each other down to the lowest temperature studied here. This suggests that $\eta = 0.18$ is close to the phase boundary between the sD-oF and sF-oAF phases. Therefore, we conclude that the ground state of the spin-orbital model \mathcal{H}_{so} undergoes a phase transition between the sD-oF and sF-oAF phases at $\eta = \eta_c \sim 0.18$. Note that this ground-state phase transition as well as the critical value $\eta_c \sim 0.18$ is in good agreement with the mean-field prediction in Sec. III A.

In the case of a finite JT coupling, we have found that there occurs a finite-temperature phase transition to the low-temperature sF-oAF phase for $\eta > \eta_c$ or to the sD-oF phase for $\eta < \eta_c$. The details will be reported elsewhere. We thus expect that the transition between the low-temperature sD-oF and sF-oAF phases by changing η is a general feature of the spin-orbital-lattice coupled model (1).

-
- ¹ Y. Tokura and N. Nagaosa, *Science* **288**, 462 (2000).
² M. Imada, A. Fujimori, and Y. Tokura, *Rev. Mod. Phys.* **70**, 1039 (1998).
³ K. I. Kugel and D. I. Khomskii, *Sov. Phys. Usp.* **25**, 231 (1982).
⁴ E. O. Wollan and W. C. Koehler, *Phys. Rev.* **100**, 545 (1955); J. B. Goodenough, *Phys. Rev.* **100**, 564 (1955).
⁵ S. Miyasaka, Y. Okimoto, M. Iwama, and Y. Tokura, *Phys. Rev. B* **68**, 100406(R) (2003).
⁶ Y. Motome, H. Seo, Z. Fang, and N. Nagaosa, *Phys. Rev. Lett.* **90**, 146602 (2003).
⁷ G. Khaliullin, P. Horsch, and A. M. Oleś, *Phys. Rev. Lett.* **86**, 3879 (2001).
⁸ M. Isobe, E. Ninomiya, A. Vasil'ev, and Y. Ueda, *J. Phys. Soc. Jpn.* **71**, 1423 (2002).
⁹ E. Ninomiya, M. Isobe, Y. Ueda, M. Nishi, K. Ohoyama, H. Sawa, and T. Ohama, *Physica B* **329-333**, 884 (2003).
¹⁰ J. W. Bray, L. V. Interrante, I. S. Jacobs, J. C. Bonner, *Extended Linear Chain Compounds* vol.3, ed. by J. C. Miller (New York, Plenum Press, 1983) p.353; J. P. Boucher and L. P. Regnault, *J. Phys. I (France)* **6**, 1939 (1996); K. Uchinokura, *J. Phys: Condens. Matter* **14**, 195 (2002).
¹¹ N. Katoh, *J. Phys. Soc. Jpn.* **68**, 258 (1999).
¹² M. J. Konstantinović, J. van den Brink, Z. V. Popović, V. V. Moshchalkov, M. Isobe, and Y. Ueda, *Phys. Rev. B* **69**, 020409(R) (2004).
¹³ K. I. Kugel and D. I. Khomskii, *Sov. Phys. Solid. State* **17**, 285 (1975).
¹⁴ P. Millet, F. Mila, F. C. Zhang, M. Mambrini, A. B. Van Oosten, V. A. Pashchenko, A. Sulpice, and A. Stepanov, *Phys. Rev. Lett.* **83**, 4176 (1999).
¹⁵ We note that the transfer integrals may be modified by the JT distortion. We neglect the small corrections in the present study.
¹⁶ H. Tsunetsugu and Y. Motome, *Phys. Rev. B* **68**, 060405(R) (2003).
¹⁷ T. Mizokawa and A. Fujimori, *Phys. Rev. B* **54**, 5368 (1996).
¹⁸ Y. Imry, P. Pincus, and D. Scalapino, *Phys. Rev. B* **12**, 1978 (1975); H. J. Schulz, *Phys. Rev. Lett.* **77**, 2790 (1996).
¹⁹ P. W. Anderson, *Phys. Rev.* **115**, 2 (1959).
²⁰ L. M. Roth, *Phys. Rev.* **149**, 306 (1966).
²¹ S. Inagaki and R. Kubo, *Int. J. Magnetism* **4**, 139 (1973); S. Inagaki, *J. Phy. Soc. Jpn.* **39**, 596 (1975).

- ²² H. Betsuyaku, Phys. Rev. Lett. **53**, 629 (1984); Prog. Theor. Phys. **73**, 319 (1985).
- ²³ V. Kataev, J. Baier, A. Möller, L. Jongen, G. Meyer, and A. Freimuth, Phys. Rev. B **68**, 140405(R) (2003).
- ²⁴ I. Yamada, H. Manaka, H. Sawa, M. Nishi, M. Isobe, and Y. Ueda, J. Phys. Soc. Jpn. **67**, 4269 (1998).
- ²⁵ Note that the results of the correlations are independent of the value of g .
- ²⁶ M. Suzuki and M. Inoue, Prog. Theor. Phys. **78**, 787 (1987); M. Inoue and M. Suzuki, Prog. Theor. Phys. **79**, 645 (1988).
- ²⁷ X. Wang and T. Xiang, Phys. Rev. B **56**, 5061 (1997).
- ²⁸ E. Carlon, M. Henkel, and U. Schollwöck, Eur. Phys. J. B **12**, 99 (1999).

This figure "fig1.jpg" is available in "jpg" format from:

<http://arxiv.org/ps/cond-mat/0404730v1>